Performance characterization of high quantum efficiency metal package photomultiplier tubes for time-of-flight and high-resolution PET applications

Guen Bae Ko and Jae Sung Lee[a)]
Department of Nuclear Medicine, Seoul National University College of Medicine, Seoul 110-744, Korea; Department of Biomedical Science, Seoul National University College of Medicine, Seoul 110-744, Korea; and Institute of Radiation Medicine, Medical Research Center, Seoul National University College of Medicine, Seoul 110-744, Korea

(Received 25 July 2014; revised 24 November 2014; accepted for publication 26 November 2014; published 5 January 2015)

Purpose: Metal package photomultiplier tubes (PMTs) with a metal channel dynode structure have several advanced features for devising such time-of-flight (TOF) and high spatial resolution positron emission tomography (PET) detectors, thanks to their high packing density, large effective area ratio, fast time response, and position encoding capability. Here, we report on an investigation of new metal package PMTs with high quantum efficiency (QE) for high-resolution PET and TOF PET detector modules.

Methods: The latest metal package PMT, the Hamamatsu R11265 series, is served with two kinds of photocathodes that have higher quantum efficiency than normal bialkali (typical QE $\approx$ 25%), super bialkali (SBA; QE $\approx$ 35%), and ultra bialkali (UBA; QE $\approx$ 43%). In this study, the authors evaluated the performance of the new PMTs with SBA and UBA photocathodes as a PET detector by coupling various crystal arrays. They also investigated the performance improvements of high QE, focusing in particular on a block detector coupled with a lutetium-based scintillator. A single $4\times4\times10$ mm^3 LYSO, a 7×7 array of $3\times3\times20$ mm^3 LGSO, a 9×9 array of $1.2\times1.2\times10$ mm^3 LYSO, and a 6×6 array of $1.5\times1.5\times7$ mm^3 LuYAP were used for evaluation. All coincidence data were acquired with a DRS4 based fast digitizer.

Results: This new PMT shows promising crystal positioning accuracy, energy and time discrimination performance for TOF, and high-resolution PET applications. The authors also found that a metal channel PMT with SBA was enough for both TOF and high-resolution application, although UBA gave a minor improvement to time resolution. However, significant performance improvement was observed in relative low light output crystals (LuYAP) coupled with UBA.

Conclusions: The results of this study will be of value as a useful reference to select PMTs for high-performance PET detectors.
[http://dx.doi.org/10.1118/1.4903897]

Key words: positron emission tomography (PET), metal package PMT, high quantum efficiency (high QE), super bialkali (SBA), ultra bialkali (UBA)

1. INTRODUCTION

Positron emission tomography (PET) allows the visualization of the *in vivo* radiotracer distribution with high sensitivity and fine spatial resolution.[1–5] Time-of-flight (TOF) measurement capability is an important feature of modern whole-body PET systems because the reconstruction of PET images using a TOF kernel results in a significant improvement in image quality.[6–8] Recent studies also have shown that the TOF information leads to improved accuracy in the joint estimation of the radioactivity distribution and attenuation coefficient map.[9,10] Also, a high spatial resolution is required in PET scanners, which are designed for scanning specific human organs, such as the brain and breast, and small animals.[11–14]

Although the silicon photomultiplier (SiPM) has gained great attention as a novel photosensor,[15–19] the photomultiplier tube (PMT) is still regarded as the most stable and mature photosensor for PET. In particular, metal package PMTs with a metal channel dynode structure have several advanced features for devising such TOF and high spatial resolution PET detectors, thanks to their high packing density, large effective area ratio, fast time response, and position encoding capability.[20–22]

The R11265 series metal package PMTs of Hamamatsu Photonics K. K. (Hamamatsu, Japan) have been recently introduced for various visible light photon detection applications.[23] More improved photocathodes for yielding high quantum efficiency (QE) are employed in the R11265 series metal package PMTs: super bialkali (SBA), and ultra bialkali (UBA) photocathodes. Although conventional bialkali (BA) photocathodes yield 25% typical QE at 350 nm wavelength, SBA and UBA photocathodes yield 35% and 43%, respectively.[24] The superior QE and sophisticated dynode structure in these PMTs would lead to improved energy and time resolution of PET detectors based on them.[25,26]

In this study, we investigated the physical performance of PET detectors based on these new R11265 series metal package PMTs that were combined with various lutetium-based scintillation crystal blocks (LYSO, LGSO, and LuYAP) and a charge-division network for position signal encoding, with the focus on the relationship between the PET detector performances and the QE of PMT in association with light yield of the scintillation crystal.

2. MATERIALS AND METHODS

2.A. PMTs and scintillators

The major characteristics of metal package PMTs evaluated in this study are summarized in Table I. The R11265-100-M16 is a 1-in. square 16-channel metal package PMT with a SBA photocathode. Another variant of R11265 series, R11265-200-M16 has identical mechanical structure with R11265-100-M16 but incorporates an UBA photocathode [Fig. 1(a)]. The new R11265 series PMTs have faster rise and transit times, and smaller transit time spread than H8500, which is the multianode flat panel PMT widely used for high-resolution PET applications. The R11265 series PMT also has a larger effective area ratio than the old version of the 1-in. square metal package PMT (R7600). In PET applications, these properties are helpful for reducing random coincidence events and improving the geometric efficiency of coincidence detection.

We compared the performance characteristics of R11265 series PMTs with those of H8500. The H8500 has similar mechanical designs including dynode structure, number of dynode stages, and photocathode cell size as the R11265 PMTs, but conventional BA photocathode is used in H8500 (Table I). Because the H8500 PMT covers 2-in. square effective area, we used only central 4×4 channels of whole 8×8 anodes [Fig. 1(c)].

The UBA PMT (R11265-200-M16) used in this study has ~1.1 times higher QE than the SBA PMT (R11265-100-M16) and ~1.5 times higher QE than the conventional BA PMT (H8500) for blue light (420 nm). Various kinds and sizes of crystal blocks shown in Fig. 1(b) were coupled with the PMTs to examine detector performance depending on QE. A single LYSO ($Lu_{1.8}Y_{0.2}SiO_5$:Ce; $4\times4\times10$ mm^3) crystal was matched with a cathode cell of the PMTs to investigate the performance related to time pickoff method and supply voltage [Fig. 3(c)]. To explore the properties of PET detectors based on these PMTs in whole-body TOF-PET and high spatial resolution PET applications, 7×7 LGSO ($Lu_{1.9}Gd_{0.1}SiO_4$:Ce; $3\times3\times20$ mm^3, pitch = 3.1 mm) and 9×9 LYSO ($1.2\times1.2\times10$ mm^3, pitch = 1.28 mm) crystal arrays were coupled at the center of effective area, respectively [Fig. 3(c)]. A 6×6 array of LuYAP ($Lu_{0.7}Y_{0.3}AlO_3$:Ce; $1.5\times1.5\times10$ mm^3, pitch = 1.6 mm) crystal was also used for evaluating the PET detectors' performance based on crystals with relatively low light yield. These crystals were coupled with PMTs via optical grease (BC630, Oken, Japan) without use of other light guides in all experiments. The results were compared to investigate the effects of QE on PET detectors' performance depending on their application.

2.B. Front-end electronics

Four multiplexed position signals (A, B, C, and D) were obtained using an Anger-like weighted summing circuit for 16 output signals from R11265 PMTs and H8500 PMT.[27] For achieving even space between the crystal peak positions in

TABLE I. Main parameters of the MA-PMTs used in the experiments (at 25 °C).

Parameter		HAMAMATSU H8500 (CA2979)	HAMAMATSU R11265 series: R11265-100-M16 (DA0041)	HAMAMATSU R11265 series: R11265-200-M16 (DA0001)
Number of anodes		64 (8×8)	16 (4×4)	
Photocathode	Material	Bialkali	Super bialkali	Ultra bialkali
	Minimum effective area	49×49 mm^2	23×23 mm^2	
	Cell size	6.08×6.08 mm^2	5.75×5.75 mm^2	
Number of stages		12	12	
Anodes luminous sensitivity		255 A/lm	214 A/lm	333 A/lm
Cathode sensitivity	Luminous sensitivity	69.6 μA/lm	110 μA/lm	125 μA/lm
	Blue sensitivity index	10.2	14.1	15.4
Quantum efficiency	at 350 nm	—[a]	—[a]	40.5%[b]
	at 380 nm	—[a]	—[a]	40.4%[b]
	at 420 nm	24.3%[c]	33.6%[c]	36.7%[b]
Time response (typical)	Rise time	0.8 ns	0.52 ns	
	Transit time	6 ns	5 ns	
	Transit time spread	0.4 ns	0.34 ns	

[a]No measured QE and sensitivity data at given wavelength.
[b]Measured by Hamamatsu Photonics K.K.
[c]Estimated from QE of R11265-200-M16 and blue sensitivity index difference.

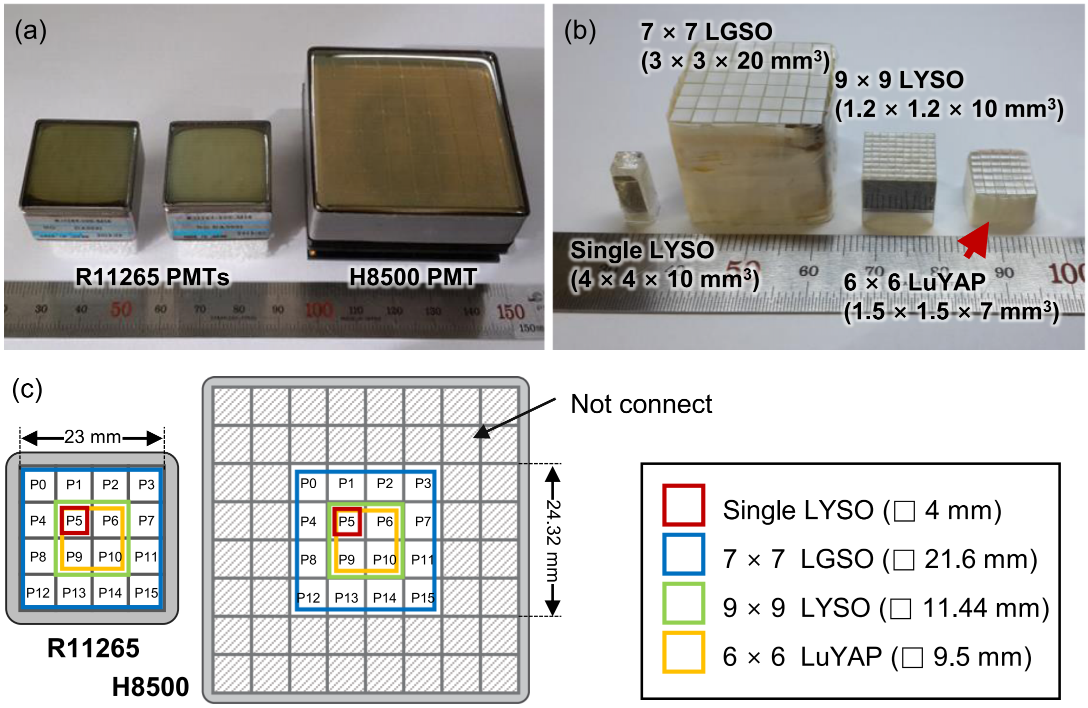

FIG. 1. (a) The R11265 series PMTs and H8500 PMT used in this paper, and (b) single crystal and crystal blocks used for evaluation. (c) Mechanical drawing of PMTs and covering area of each crystal blocks.

flood image, the weighing values are determined as follows. The position of anode signal is indicated in Fig. 1(c).

$$A = P0+\frac{2}{3}P1+\frac{1}{3}P2+\frac{2}{3}P4+\frac{2}{5}P5+\frac{1}{4}P6+\frac{1}{3}P8 +\frac{1}{4}P9+\frac{1}{10}P10, \tag{1}$$

$$B = P3+\frac{2}{3}P2+\frac{1}{3}P1+\frac{2}{3}P7+\frac{2}{5}P6+\frac{1}{4}P5+\frac{1}{3}P11 +\frac{1}{4}P10+\frac{1}{10}P9, \tag{2}$$

$$C = P15+\frac{2}{3}P14+\frac{1}{3}P13+\frac{2}{3}P11+\frac{2}{5}P10+\frac{1}{4}P9 +\frac{1}{3}P7+\frac{1}{4}P6+\frac{1}{10}P5, \tag{3}$$

$$D = P12+\frac{2}{3}P13+\frac{1}{3}P14+\frac{2}{3}P8+\frac{2}{5}P9+\frac{1}{4}P10 +\frac{1}{3}P4+\frac{1}{4}P5+\frac{1}{10}P6. \tag{4}$$

The interaction position of the gamma ray used for flood image and crystal map generation was then calculated using the following equations:

$$X = \frac{A+D-B-C}{A+B+C+D}, \tag{5}$$

$$Y = \frac{A+B-C-D}{A+B+C+D}. \tag{6}$$

The multiplexed position signals and dynode signal (signal from 12th dynode) were amplified by preamplifiers (gain $\approx$ 2–3.1, see Sec. 2.C). The dynode signal was fed into three second stage amplifiers: two low gain amplifiers (gain $\approx$ 2) to generate signals used for energy measurement and triggering and one high gain amplifier (gain $\approx$ 10) for extracting a precise photon arrival time information (Fig. 2). To minimize the bandwidth reduction of amplifiers due to the raised gain, a high speed current feedback amplifier (AD8000; Analog Device, Inc., MA) was used; the bandwidth of cascade amplifier for time signal was 365 MHz, limited by second stage high gain amplifier.[28] This bandwidth was sufficiently wide to maintain the rising edge of the PMT signal.

2.C. Data acquisition setup

A reference detector that consisted of a LYSO crystal ($4\times4\times10$ mm^3) and a Hamamatsu R9800 fast PMT was used for coincidence data acquisition. The signal from reference detector was fed into the amplifiers which are same as the second stage amplifiers explained in Sec. 2.B. The detectors were irradiated using a 4.9 μCi ^{22}Na point source that was located 15 cm away from the R11265/H8500 PMT detector surface and just in front of the reference detector. The coincidence trigger signal was generated from the dynode signal of the R11265/H8500 PMT and the anode signal of the reference R9800 PMT (Fig. 2).

The signals from the PMTs were acquired using a DRS4 based high speed waveform digitizer (DT5742; CAEN, Italy), a kind of switched capacitor array that is less expensive and requires lower power consumption than a conventional flash structure ultrahigh speed analog-to-digital convertor (ADC).[29,33] The sampling rate of DT5742 is 5 Giga samples/s, and the sampling resolution is 12-bit for each channel.

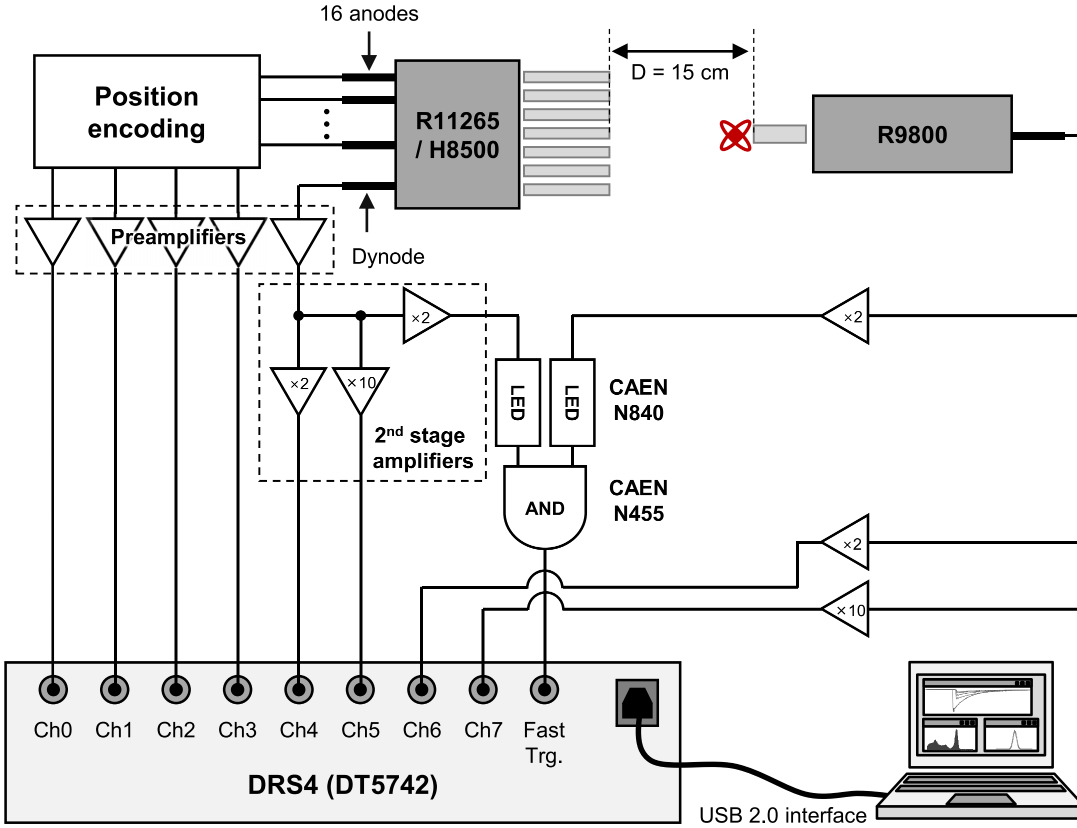

FIG. 2. Schematic of experimental setup to acquire coincidence data with high speed digitizer.

The time resolution measured based on the waveform digitizer is degraded by not only electronic noise but also by quantization and interpolation errors. The quantization error depends on the sampling bit of the ADC and the amplitude of the analog signal, which is mainly determined by the light output from the scintillation crystal and the gain of the photosensor and amplifier. The interpolation error is associated with the signal interpolation method, ADC sampling rate, and slope of the analog signal determined by the decay time of the scintillation crystal, the rise time of the PMT, and the bandwidth of the amplifier. For these reasons, to achieve good time resolution and to make a fair comparison, the amplification gain of the preamplifiers (indicated in Fig. 2) was set differently depending on the PMT and scintillation crystals to obtain a sufficiently high and similar scintillation pulse at a peak amplitude of 511 keV. According to the anode luminous sensitivity difference of PMTs used in this study (Table I), the gain of preamplifiers for BA, SBA, and UBA

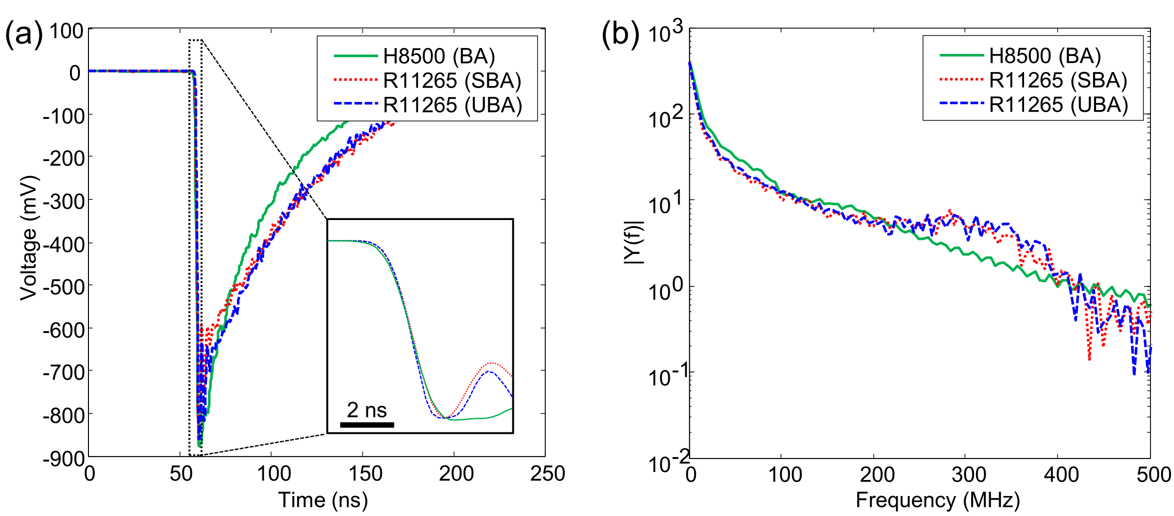

FIG. 3. (a) Averaged output pulse with $4 \times 4 \times 10$ mm^3 LYSO crystal, (b) Fourier transform of output pulses at 1000 V supply voltage. The inset in (a) shows the detail of the rise part.

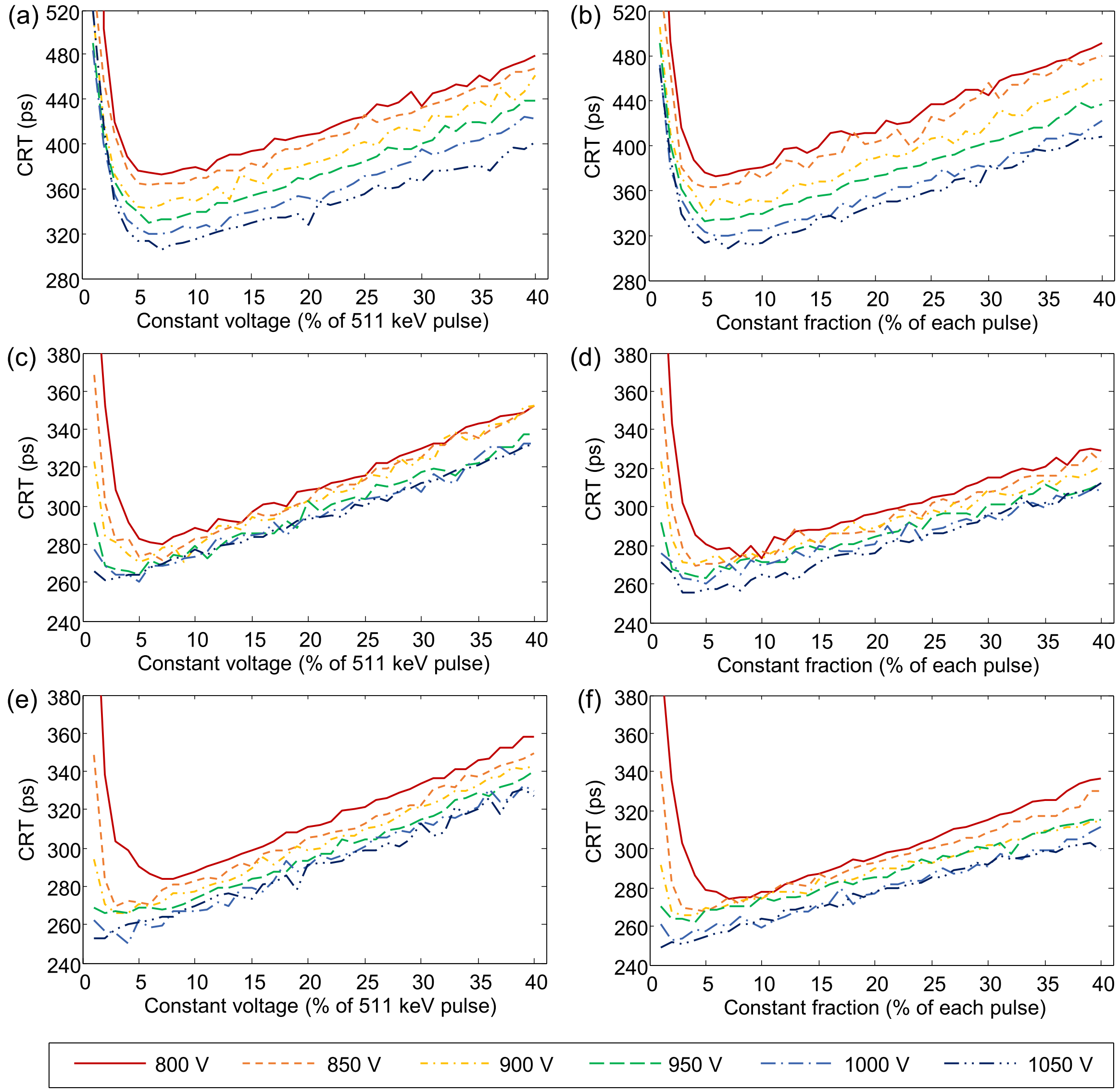

Fig. 4. Time resolution dependence against the time pickoff method and PMT supply voltage. (a) CRT of BA PMT measured by constant voltage threshold, (b) CRT of BA PMT measured by constant fraction threshold, (c) CRT of SBA PMT measured by constant voltage threshold, (d) CRT of SBA PMT measured by constant fraction threshold, (e) CRT of UBA PMT measured by constant voltage threshold, and (f) CRT of UBA PMT measured by constant fraction threshold.

PMTs were set to 2.6, 3.1, and 2.0, respectively, to yield similar pulse amplitude.

2.D. Performance evaluation and data analysis

The performance dependency on the PMT supply voltage and digital time pickoff method was evaluated using a single LYSO ($4\times4\times10$ mm^3) crystal positioned at the center of one PMT cell. We changed the PMT supply voltage from 800 to 1050 V and tested two time pickoff methods: constant voltage and constant fraction. The threshold voltage of the constant voltage and constant fraction methods was changed from 1% to 40% in 1% step of the 511 keV pulse and of the individual pulse amplitude, respectively. Data were acquired repeatedly five times for each PMT, and each data set included 30 000 coincidence events.

For the block detector performance evaluation, we set the supply voltage of the PMT to 1000 V and used constant fraction method with a 6% threshold for BA PMT and with a 2% threshold for SBA and UBA PMTs according to the results of single crystal evaluation. Two million coincidence events were acquired for each crystal block and PMT pair, and the flood image and energy resolution (dE/E) and coincidence resolving time (CRT) of individual crystals were evaluated. The individual crystals in the flood images were identified by automatic procedures. First, the flood images were smoothed by Gaussian filter, and proper thresholds which separate crystals from background were calculated using Otsu's method. The position of each crystal was extracted applying the threshold, and the flood images were partitioned by Voronoi decomposition.

As a figure-of-merit of flood image quality, distance-to-width ratio (DWR) which is defined as the ratio of separation between two adjacent spots in the flood images to the average full-width-half-maximum (FWHM) of the two spots was calculated.[31,32]

We also conducted paired t-tests on the dE/E, CRT, and DWR to evaluate whether the differences between them as a result of different QEs are statistically significant.

All time information was extracted from the digitalized pulse after baseline correction and cubic spline interpolation by a factor of 10 to measure accurate arrival time. The energy window used for all time resolution measurement was ±20% of 511 keV (409–613 keV). All time resolution values expressed in this paper are predicted CRT $\left(\Delta t_{R11265/R11265}\right)$ of each PMT by quadratically subtracting the time uncertainty of the reference PMT from measured time resolution with reference detector $\left(\Delta t_{R11265/\mathrm{Ref}}\right)$ and multiplying with $\sqrt{2}$ as indicated in following equation:

$$\Delta t_{R11265/R11265} = \sqrt{2}\sqrt{\left(\Delta t_{R11265/\mathrm{Ref}}\right)^2 - \left(\delta t_{\mathrm{Ref}}\right)^2}. \quad (7)$$

The time uncertainty of the R9800 reference PMT (δt_{Ref}), which was measured with two other PMT detectors and the DRS4 based acquisition system, was ∼190 ps.

3. RESULTS

3.A. Output pulse signal properties of new metal package PMTs

The signal in Fig. 3(a) is the average of 64 typical 511 keV fast timing signals (output of high gain amplifier) from the PMTs with a single LYSO crystal that is sampled by a DRS4 based digitizer applying a very narrow energy window (±1%). The rise times (10%–90%) of the scintillation pulse were 1.68 ± 0.33 ns, 1.26 ± 0.21 ns, and 1.24 ± 0.10 ns for the conventional BA, SBA, and UBA type PMTs, respectively. The dominant factor that determines time resolution, dV/dt, of rise part was not different between the two R11265 PMTs. Although the decay parts were slightly different, they do not seem to be significant. The rise and decay times of the pulse generated from BA PMT (H8500) were different from those of R11265 PMTs which might be caused by unequal mechanical structure and electrical properties (i.e., voltage divider circuits).

There was also no significant difference between two R11265 PMTs in the frequency domain, as shown in the Fourier transform of the scintillation pulse [Fig. 3(b)], indicating that the bandwidth of the amplifier was sufficient for conserving the signal slope from the PMT. The BA PMT (H8500) had smaller high frequency component as we expected from the shape of scintillation pulse.

3.B. Performance according to PMT gain and time pickoff methods

Since the timing and energy performances of the detectors were influenced by the PMT supply voltage and time pickoff methods, we checked the optimal setup using the PMTs coupled with a single 10-mm length LYSO crystal.

Figure 4 illustrates the CRT as a function of the supply voltage, time pickoff method, and pickoff threshold level for H8500-BA [Figs. 4(a) and 4(b)], R11265-SBA [Figs. 4(c) and 4(d)], and R11265-UBA [Figs. 4(e) and 4(f)] PMTs. In all PMT types, constant voltage and fraction methods yielded similar pattern of CRT curves as shown in Fig. 4. However, when the threshold level increased, the constant fraction method yielded better CRT mainly because the constant voltage method with high threshold level suffers severe time-walk error. In both cases, the CRT with a low threshold was better when the PMT was supplied adequately high voltage. In the case of low supply voltage, low threshold yielded poor time resolution because a low threshold tends to lead to unreliable time picking caused by noise when the signal-to-noise ratio (SNR) of the signal is not sufficient. The optimal threshold level to yield best CRT was 5%–10% for

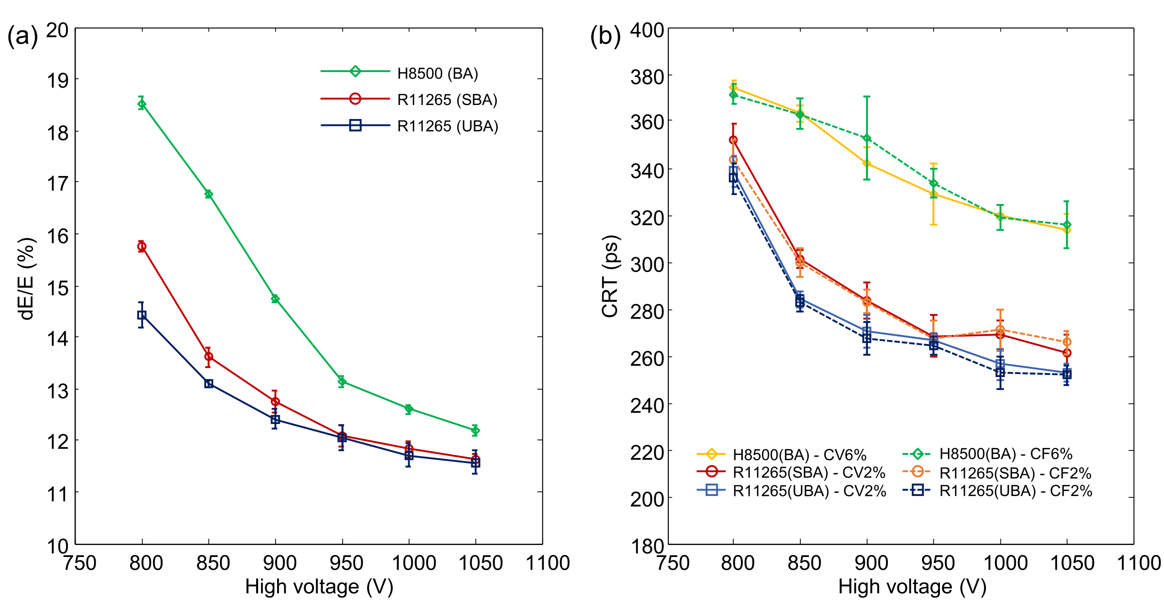

FIG. 5. (a) Energy resolution dependency and (b) time resolution dependency on the gain of the PMT.

BA PMT and 2%–5% for SBA and UBA PMTs with the sufficiently high supply voltage regardless of time pickoff method.

Figure 5(a) shows the measured energy resolution for a 511 keV scintillation pulse at the various PMT supply voltages. The energy resolution tended to improve with an increase in supply voltage. The CRT of each PMT obtained using the constant voltage and constant fraction methods with a 2% threshold for SBA and UBA PMTs and 6% for BA PMT also improved with increasing supply voltage, as shown in Fig. 5(b). These improvements of time and energy resolutions can be partially attributed to the decreasing quantization error based on increased PMT gain with increasing supply voltage. However, when the supply voltage was set above 1000 V, energy and time resolutions of SBA and UBA PMTs showed no significant change with the supply voltage.

We also found that the SBA and UBA PMTs apparently improved both the CRT and energy resolution compared to the conventional BA PMT. In the comparison of the SBA and UBA, the UBA showed slightly better CRT, but similar energy resolution. The results are in overall agreement with those predicted from their quantum efficiency differences.

3.C. Performance of block detector

Figures 6, 7, and 8 show the flood image and energy and time resolution distributions of the crystals in the 7×7 LGSO, 9×9 LYSO, and 6×6 LuYAP crystal array, respectively. In all flood images, the crystals are clearly resolved with high peak-to-valley. Results of the quantitative analysis are summarized in Table II.

The SBA PMT yielded significantly ($P < 0.001$) improved energy resolution, CRT, and DWR than BA PMT in all cases. In the comparison between SBA and UBA, energy resolution and DWR were almost identical in coupling with 7×7 LGSO and 9×9 LYSO arrays, which are the demonstrations of TOF PET and small animal PET detectors, respectively. The SBA photocathode generates sufficiently large number of photons which make other factors such as intrinsic scintillator performance, coupling, and system noise more dominant than error due to the photon counting statistics. Only the CRT was signif-

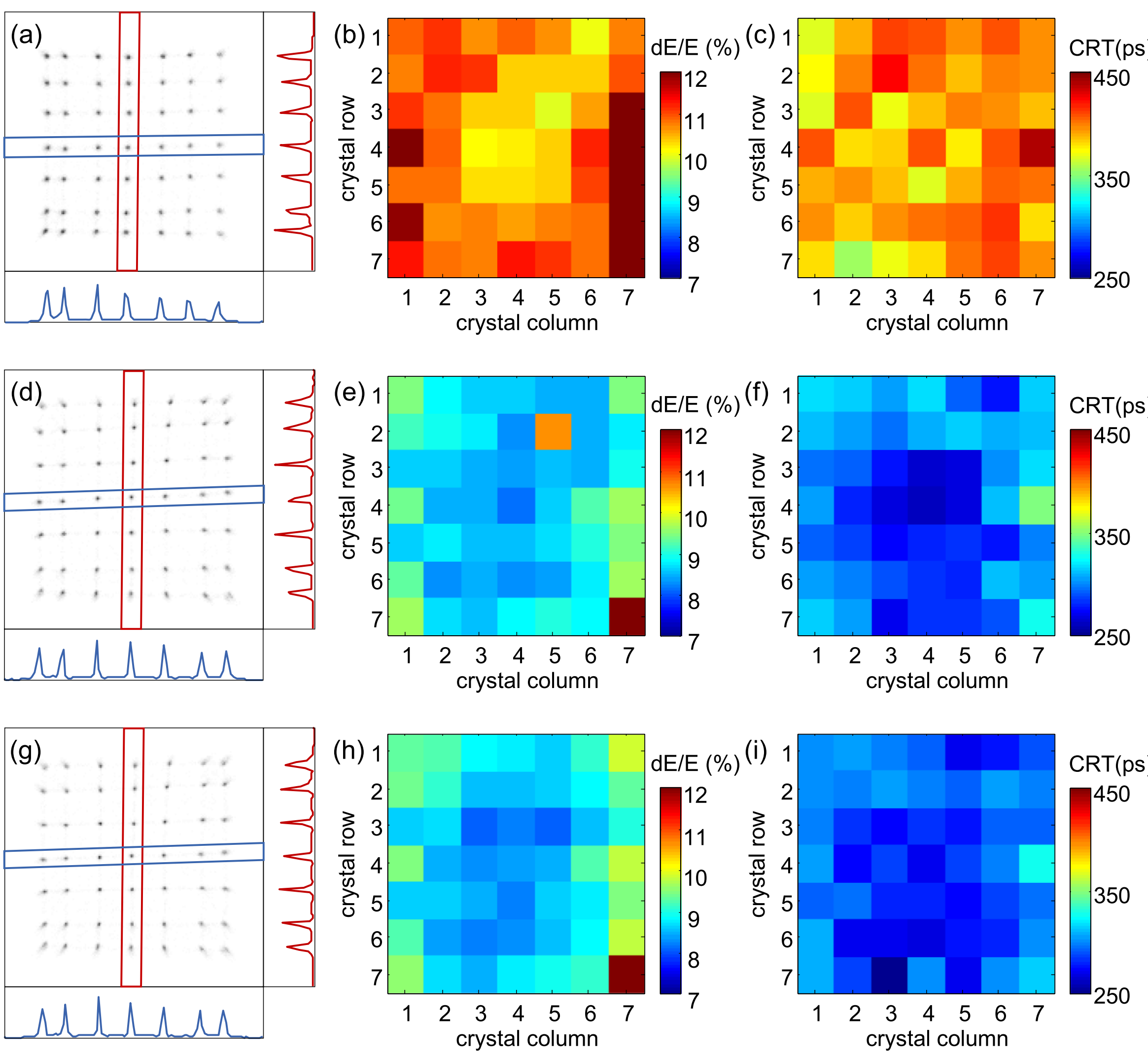

Fig. 6. Flood image and energy and time resolution distributions of 49 crystals of 3 mm LGSO block by coupling [(a)–(c)] BA PMT, [(d)–(f)] SBA PMT, and [(g)–(i)] UBA PMT.

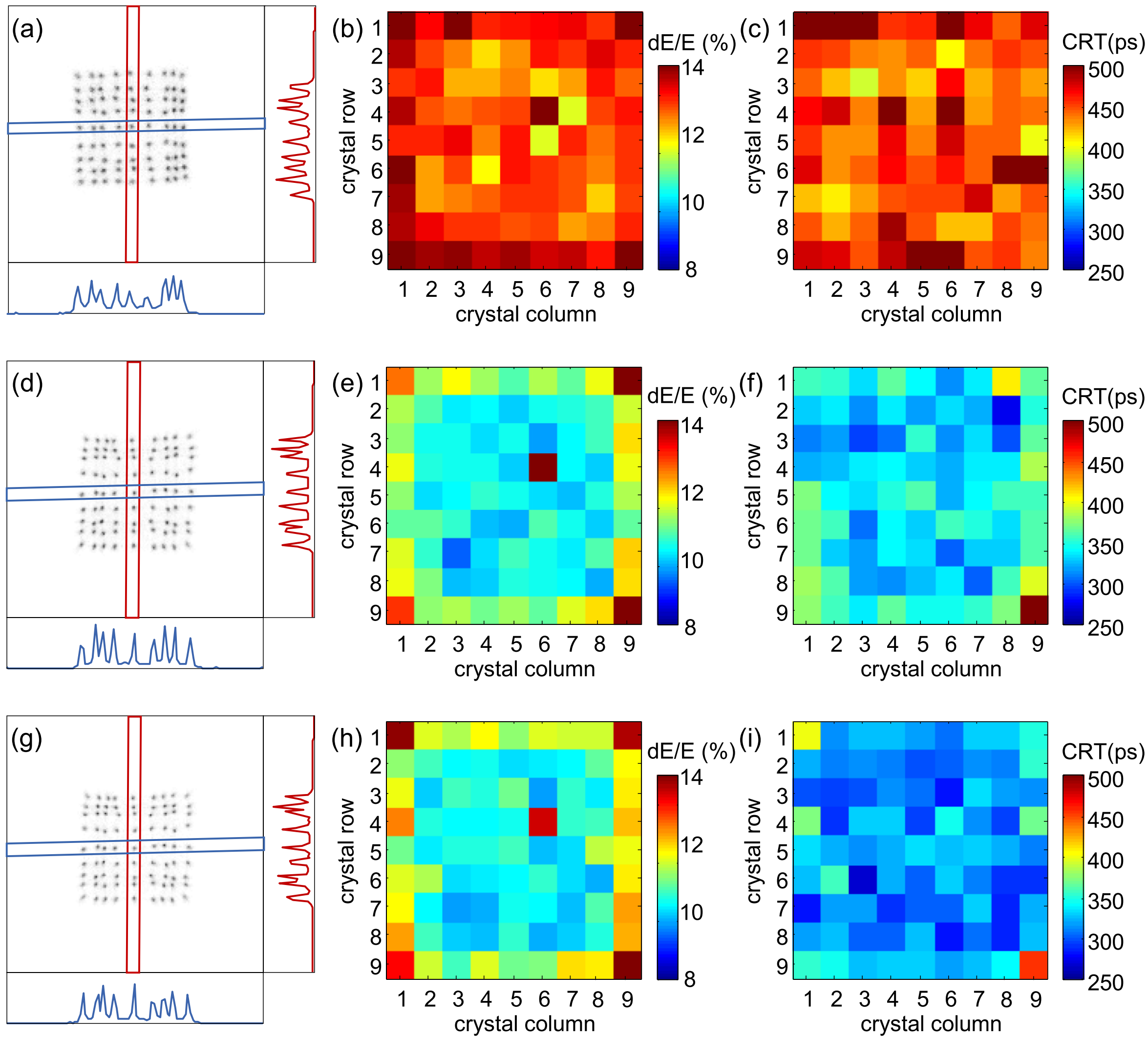

FIG. 7. Flood image and energy and time resolution distributions of 81 crystals of 1.2 mm LYSO block by coupling [(a)–(c)] BA PMT, [(d)–(f)] SBA PMT, and [(g)–(i)] UBA PMT.

icantly improved, but the improvement was not remarkable. Interestingly, the UBA PMT yielded much better performance than the SBA PMT in the coupling with the LuYAP array. It would be interpreted that the enhancement of PET detector performance by QE improvement was increased in accordance with the decrease of light output from the scintillation crystal.

Evaluation of detector performance according to the position on PMT window is important because performance degradation is expected near the edge of PMT window. From the results of 7×7 LGSO array which covers almost the entire PMT effective area, we found that the energy resolution and CRT were degraded near the edge and corner of the PMT where the light collection efficiency is worse than the center [Figs. 6(e), 6(f), 6(h), and 6(i)].

4. DISCUSSION

It is well recognized that the energy and time resolving powers of gamma-ray detectors are affected by several factors, such as how fast and bright the scintillator is, how fast and accurate the electrical pulse of photosensor is, and how efficient the coupling is. This paper has attempted to investigate the effect of an advanced metal package PMT on PET block detector performance with a high-speed waveform digitizer. The superior QE, collection efficiency, and transit time spread of these new metal package PMTs were effective in improving the gamma event discrimination performance.

With a 3 mm crystal block, the average measured CRT and energy resolution of new R11265 PMTs across the 49 crystals showed promising results. However, the results were a little worse than the CRT of a P-on-N type SiPM with an identical size of LYSO scintillation crystal ($3\times3\times20$ mm^3) and the same digital triggering methods.[33] In spite of this, our results indicate that the new metal package PMT is a strong candidate for next-generation TOF PET development, because the LYSO-SiPM result was measured using a pair of single SiPM and LYSO elements. A recent study showed that the optical cross talk between the crystals due to the reflector and epoxy window of SiPM degraded timing performance even if the detector consisted of a multielement one-to-one coupled LYSO-SiPM array with individual readouts.[30]

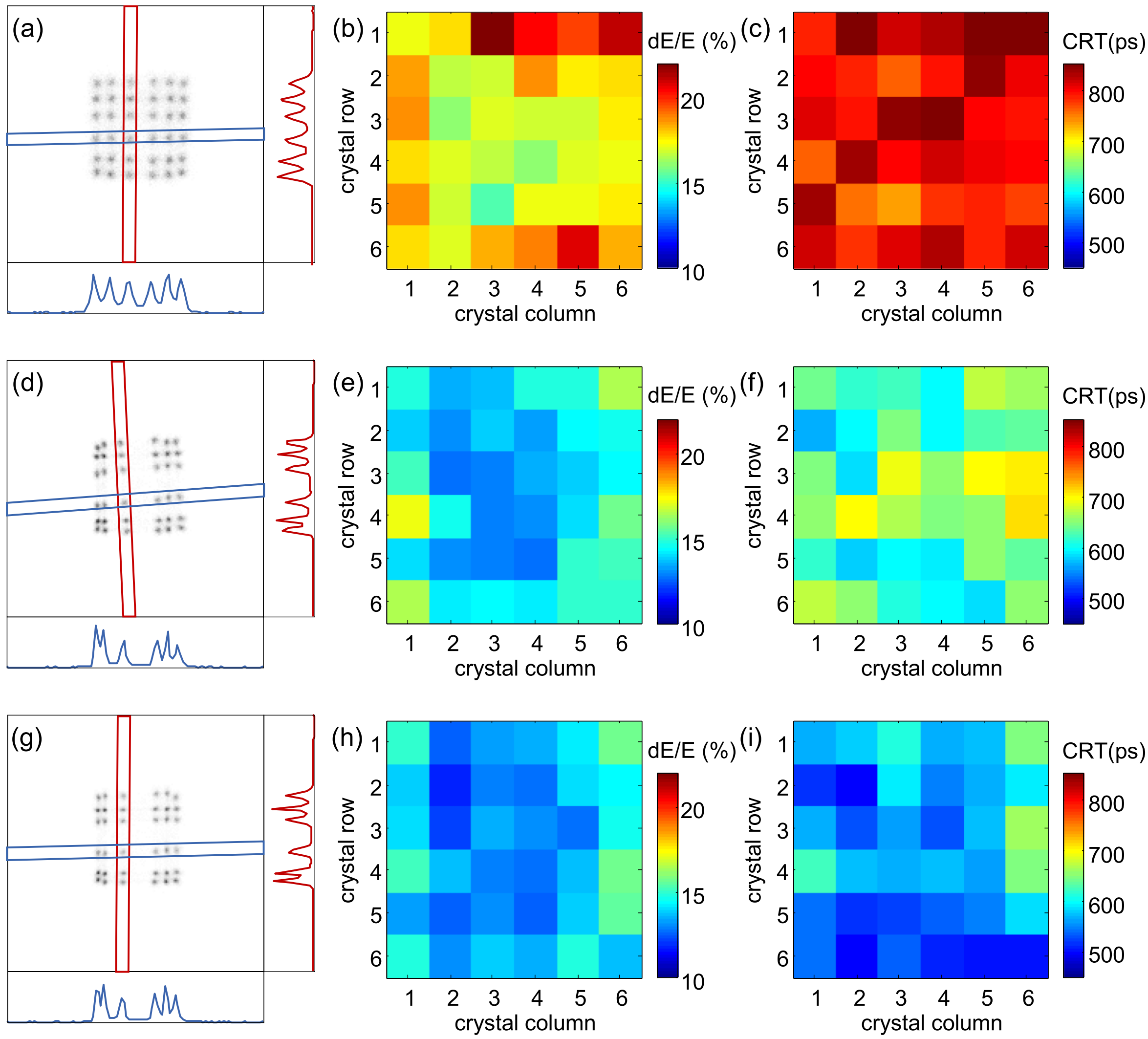

FIG. 8. Flood image and energy and time resolution distributions of 36 crystals of 1.5 mm LuYAP block by coupling [(a)–(c)] BA PMT, [(d)–(f)] SBA PMT, and [(g)–(i)] UBA PMT.

It is well known that better QE leads to better detector performance. However, the degree of improvements also relies on several other factors, including the scintillation type and size, and the coupling method between the scintillator and photosensor. The following equation describes such relationships between the detector performances and various physical and technical factors:[34]

$$\left(\frac{\Delta E}{E}\right)^2 \approx \delta_0^2 + \frac{1}{N_0}\frac{1}{QE}\frac{1}{\alpha_{\text{coupling}}} + \delta_{\text{ADC}}^2 + \delta_{\text{noise}}^2, \tag{8}$$

$$\tau^2 \approx \tau_0^2 \frac{1}{N_0}\frac{1}{QE}\frac{1}{\alpha_{\text{coupling}}} + \Delta\tau_{\text{PL}}^2 + \Delta\tau_{\text{PMT}}^2 + \Delta\tau_{\text{DISCR}}^2 + \Delta\tau_{\text{TDC}}^2 + \Delta\tau_{\text{noise}}^2. \tag{9}$$

In the equation, δ_0 and τ_0 represent the intrinsic energy resolution and intrinsic time resolution of the scintillator, properties that are determined by the scintillator materials. The other term, N_0 is the scintillator's absolute light yield, and α_{coupling} is the light transmission factor in the crystals and block structure. These terms are related to the number of photoelectrons detected at the PMT photocathode and determine the Poisson statistical error. The other terms in the equation denote the time jitter from light dispersion in the scintillator and light guide ($\Delta\tau_{\text{PL}}$), the transit time spread of the PMT ($\Delta\tau_{\text{PMT}}$), the discriminator and acquisition (δ_{ADC}, $\Delta\tau_{\text{DISCR}}$, and $\Delta\tau_{\text{TDC}}$), and other system noise (δ_{noise} and $\Delta\tau_{\text{noise}}$). The improvement of QE, $\Delta\tau_{\text{PMT}}$, even α_{coupling}, and $\Delta\tau_{\text{PL}}$ can be predicted in the new metal package PMT.

In all detectors tested in this study, SBA photocathode led to remarkably improved PET detector performance relative to conventional BA PMT. This implies that the Poisson statistics is a dominant factor in determining the performance of PET detector consisting of BA PMT. These results are also in agreement with recent other studies.[32,35]

The SBA or UBA should be selected according to the application. In the case of the 3 mm crystal array for TOF application, the amount of photoelectrons generated by the SBA photocathode [approximately 5 400 photons, calculated from the QE and light yield of LYSO, 30 000 photons/MeV (Ref. 36)] was large enough to produce a lower dominant statistical error. Accordingly, the 1.1 times QE improvement achieved by adopting UBA PMT (33.6%–36.7%) did not

TABLE II. Summary of block detector performance measurements.

Crystal array	$\Delta E/E$ (%) H8500 (BA)	$\Delta E/E$ (%) R11265 (SBA)	$\Delta E/E$ (%) R11265 (UBA)	CRT (ps) H8500 (BA)	CRT (ps) R11265 (SBA)	CRT (ps) R11265 (UBA)	Average DWR H8500 (BA)	Average DWR R11265 (SBA)	Average DWR R11265 (UBA)
7 × 7 LGSO	10.17 ± 0.74[a]	8.92 ± 0.93	8.92 ± 0.93	380.70 ± 16.08[a]	296.54 ± 18.48	290.25 ± 14.35[b]	7.48 ± 1.57[a]	8.99 ± 2.57	9.06 ± 2.96
9 × 9 LYSO	13.52 ± 0.99[a]	11.33 ± 1.40	11.40 ± 1.22	443.14 ± 24.14[a]	335.37 ± 19.82	315.09 ± 18.22[a]	3.20 ± 0.80[a]	3.99 ± 1.24	4.06 ± 1.26
6 × 6 LuYAP	17.89 ± 1.53[a]	14.26 ± 1.10	13.67 ± 1.01[a]	804.48 ± 30.49[a]	615.94 ± 38.83	558.91 ± 41.70[a]	2.62 ± 0.63[a]	3.51 ± 1.67	3.86 ± 1.95[b]

[a]Statistically significant ($P < 0.001$ vs SBA).
[b]Statistically significant ($P < 0.01$ vs SBA).

significantly influence the overall performance. Moreover, less improvement could be predicted from the recently spotlighted $LaBr_3$ scintillator [light yield ≈58 000 photons/MeV (Ref. 36)] for TOF applications, which is twice as bright as the L(Y or G)SO. Therefore, it is reasonable to suppose that the SBA metal package PMT is sufficient for a whole-body TOF PET detector coupled with a few centimeter tall scintillator.

The visible light photons generated by the photoelectric effect or by Compton scattering have more chance to reflect on the surface in a small crystal than in a large crystal. This phenomenon reduces the amount of visible light photons that can be detected at the PMT photocathode, which is why the 33% QE (SBA) was not enough to obtain the best time resolution in the high-resolution PET detector ($1.2 \times 1.2 \times 10$ mm^3), unlike in the TOF PET detector ($3.0 \times 3.0 \times 20$ mm^3). However, the gain in the TOF information is not significant for imaging a relatively small object like a specific organ or a small animal because the SNR improvement due to TOF is directly proportional to the square root of object diameter and inversely proportional to the square root of position uncertainty determined by time resolution. Thus, we conclude that the SBA metal package PMT is still enough in most high-resolution PET applications.

In contrast to L(G or Y)SO which has peak emission wavelength at blue light region (420 nm), LuYAP has the peak at shorter wavelength, 350–380 nm.[36] In addition, the light output [N_0 in Eqs. (8) and (9)] of the LuYAP is also three to four times smaller than that of the LGSO and LYSO.[36,37] Therefore, even though the QEs of these metal package PMTs at 350–380 nm are higher than at 420 nm (see Table I),[35] the number of photoelectrons produced in the PMTs coupled with LuYAP is almost three times smaller than those with similar-sized LYSO crystal in our experiments. This would result in the overall performance degradation and make significant difference between SBA and UBA PMTs (4.3% and 10.2% improvements in energy and time resolutions) contrary to the results of other scintillators. Assuming that the QE of UBA PMT is 1.1 times higher than that of SBA PMT at 380 nm, the maximum improvement (consider only Poisson error term, $\propto 1/\sqrt{\text{QE}}$) of energy and time resolutions predicted by Eqs. (8) and (9) is ∼5%. However, the improvement of time resolution is much higher than the prediction. It is probable that the QE difference at 380 nm was bigger than 1.1 times, and the coupling condition was not identical.

5. CONCLUSION

The new type of metal channel PMT shows a promising timing and position resolving performance as a high-performance PET detector, especially for TOF and high-resolution PET applications. With these PMT and a high-speed waveform digitizer, we obtained sub-300 ps time resolution for a 3 mm element block detector. The SBA photocathode was enough for a TOF PET detector with L(G or Y)SO scintillator; however, UBA helped to improving the time resolving power for high-resolution PET development. This study lays the foundation for future work on high-performance PET system development.

ACKNOWLEDGMENT

This work was supported by grants from the National Research Foundation of Korea (NRF) funded by the Korean Ministry of Science, ICT and Future Planning (Grant No. NRF-2014M3C7034000), and the Korea Health Technology R&D Project through the Korea Health Industry Development Institute (KHIDI), funded by the Ministry of Health and Welfare, Republic of Korea (Grant No. HI14C1135). The authors would like to thank Miles Nakamura (Hamamatsu Photonics K.K.) for useful information and discussion about new metal package PMTs.

[a)]Author to whom correspondence should be addressed. Electronic mail: jaes@snu.ac.kr; Telephone: 822-2072-2938; Fax: 822-745-2938.
[1]W. A. Weber, "Monitoring tumor response to therapy with 18F-FLT PET," J. Nucl. Med. **51**, 841–844 (2010).
[2]S. J. Woo *et al.*, "Imaging of activated cortical areas after light and electrical stimulation of the rabbit retina: F-18 FDG PET-guided brain mapping," Biomed. Eng. Lett. **2**, 111–117 (2012).
[3]H.-J. Im, Y. K. Kim, Y.-i. Kim, J. J. Lee, W. W. Lee, and S. E. Kim, "Usefulness of combined metabolic–volumetric indices of 18F-FDG PET/CT for the early prediction of neoadjuvant chemotherapy outcomes in breast cancer," Nucl. Med. Mol. Imaging **47**, 36–43 (2013).
[4]C. Kim, H. H. Chung, S. W. Oh, K. W. Kang, J.-K. Chung, and D. S. Lee, "Differential diagnosis of borderline ovarian tumors from stage I malignant

ovarian tumors using FDG PET/CT," Nucl. Med. Mol. Imaging **47**, 81–88 (2013).

[5]S.-h. Lee and H. Park, "Parametric response mapping of longitudinal PET scans and their use in detecting changes in Alzheimer's diseases," Biomed. Eng. Lett. **4**, 73–79 (2014).

[6]S. Surti, A. Kuhn, M. E. Werner, A. E. Perkins, J. Kolthammer, and J. S. Karp, "Performance of Philips Gemini TF PET/CT scanner with special consideration for its time-of-flight imaging capabilities," J. Nucl. Med. **48**, 471–480 (2007).

[7]J. S. Karp, S. Surti, M. E. Daube-Witherspoon, and G. Muehllehner, "Benefit of time-of-flight in PET: Experimental and clinical results," J. Nucl. Med. **49**, 462–470 (2008).

[8]J. S. Lee and J. H. Kim, "Recent advances in hybrid molecular imaging systems," Semin. Musculoskeletal Radiol. **18**, 103–122 (2014).

[9]M. Conti, "Why is TOF PET reconstruction a more robust method in the presence of inconsistent data?," Phys. Med. Biol. **56**, 155–168 (2011).

[10]M. Defrise, A. Rezaei, and J. Nuyts, "Time-of-flight PET data determine the attenuation sinogram up to a constant," Phys. Med. Biol. **57**, 885–899 (2012).

[11]S. Cherry *et al.*, "MicroPET: A high resolution PET scanner for imaging small animals," IEEE Trans. Nucl. Sci. **44**, 1161–1166 (1997).

[12]T. Yamaya, E. Yoshida, T. Obi, H. Ito, K. Yoshikawa, and H. Murayama, "First human brain imaging by the jPET-D4 prototype with a pre-computed system matrix," IEEE Trans. Nucl. Sci. **55**, 2482–2492 (2008).

[13]S. L. Bowen *et al.*, "Initial characterization of a dedicated breast PET/CT scanner during human imaging," J. Nucl. Med. **50**, 1401–1408 (2009).

[14]M. Bergeron *et al.*, "Performance evaluation of the LabPET APD-based digital PET scanner," IEEE Trans. Nucl. Sci. **56**, 10–16 (2009).

[15]D. R. Schaart *et al.*, "LaBr3: Ce and SiPMs for time-of-flight PET: Achieving 100 ps coincidence resolving time," Phys. Med. Biol. **55**, N179–N189 (2010).

[16]C. L. Kim, D. L. Mcdaniel, and A. Ganin, "Time-of-flight PET detector based on multi-pixel photon counter and its challenges," IEEE Trans. Nucl. Sci. **58**, 3–8 (2011).

[17]T. Yamaya *et al.*, "A SiPM-based isotropic-3D PET detector X'tal cube with a three-dimensional array of 1 mm^3 crystals," Phys. Med. Biol. **56**, 6793–6807 (2011).

[18]S. I. Kwon *et al.*, "Development of small-animal PET prototype using silicon photomultiplier (SiPM): Initial results of phantom and animal imaging studies," J. Nucl. Med. **52**, 572–579 (2011).

[19]H. S. Yoon *et al.*, "Initial results of simultaneous PET/MRI experiments with an MRI-compatible silicon photomultiplier PET scanner," J. Nucl. Med. **53**, 608–614 (2012).

[20]M. Watanabe *et al.*, "A high resolution animal PET scanner using compact PS-PMT detectors," IEEE Trans. Nucl. Sci. **44**, 1277–1282 (1997).

[21]S. Majewski, V. Popov, R. Wojcik, and A. Weisenberger, "Optimization of a mini-gamma camera based on a 2×2 array of Hamamatsu H8500 PSPMTs," Nucl. Instrum. Methods Phys. Res., Sect. A **569**, 215–219 (2006).

[22]C. M. Lee *et al.*, "A novel compensation method for the anode gain non-uniformity of multi-anode photomultiplier tubes," Phys. Med. Biol. **57**, 191–207 (2012).

[23]M. Nerina cinti *et al.*, "Spectrometric performances of high quantum efficiency multi and single anode PMTs coupled to LaBr3 (Ce) crystal," Nucl. Instrum. Methods Phys. Res., Sect. A **724**, 27–33 (2013).

[24]K. Nakamura, Y. Hamana, Y. Ishigami, and T. Matsui, "Latest bialkali photocathode with ultra high sensitivity," Nucl. Instrum. Methods Phys. Res., Sect. A **623**, 276–278 (2010).

[25]T. Szczesniak, M. Moszynski, L. Swiderski, A. Nassalski, P. Lavoute, and M. Kapusta, "Fast photomultipliers for TOF PET," in *IEEE Nuclear Science Symposium Conference Record* (IEEE, Honolulu, HI, 2007), Vol. 4, pp. 2651–2659.

[26]M. Ito, J. P. Lee, and J. S. Lee, "Timing performance study of new fast PMTs with LYSO for time-of-flight PET," IEEE Trans. Nucl. Sci. **60**, 30–37 (2013).

[27]A. Kolb, E. Lorenz, M. S. Judenhofer, D. Renker, K. Lankes, and B. J. Pichler, "Evaluation of Geiger-mode APDs for PET block detector designs," Phys. Med. Biol. **55**, 1815–1832 (2010).

[28]Analog Devices, AD8000: 1.5 GHz Ultrahigh Speed Op Amp, 2013.

[29]S. Ritt, R. Dinapoli, and U. Hartmann, "Application of the DRS chip for fast waveform digitizing," Nucl. Instrum. Methods Phys. Res., Sect. A **623**, 486–488 (2010).

[30]J. Y. Yeom, R. Vinke, V. C. Spanoudaki, K. J. Hong, and C. S. Levin, "Readout Electronics and Data Acquisition of a Positron Emission Tomography Time-of-Flight Detector Module With Waveform Digitizer," IEEE Trans. Nucl. Sci. **60**, 3735–3741 (2013).

[31]J. Du *et al.*, "A simple capacitive charge-division readout for position-sensitive solid-state photomultiplier arrays," IEEE Trans. Nucl. Sci. **60**, 3188–3197 (2013).

[32]Y. Hirano *et al.*, "Performance evaluation of a depth-of-interaction detector by use of position-sensitive PMT with a super-bialkali photocathode," Radiol. Phys. Technol. **7**, 57–66 (2014).

[33]J. Y. Yeom, R. Vinke, and C. S. Levin, "Optimizing timing performance of silicon photomultiplier-based scintillation detectors," Phys. Med. Biol. **58**, 1207–1220 (2013).

[34]M. Conti, "Improving time resolution in time-of-flight PET," Nucl. Instrum. Methods Phys. Res., Sect. A **648**, S194–S198 (2011).

[35]S. Yamamoto, H. Watabe, K. Kato, and J. Hatazawa, "Performance comparison of high quantum efficiency and normal quantum efficiency photomultiplier tubes and position sensitive photomultiplier tubes for high resolution PET and SPECT detectors," Med. Phys. **39**, 6900–6907 (2012).

[36]M. Conti, L. Eriksson, H. Rothfuss, and C. L. Melcher, "Comparison of fast scintillators with TOF PET potential," IEEE Trans. Nucl. Sci. **56**, 926–933 (2009).

[37]S. Weber, D. Christ, M. Kurzeja, R. Engels, G. Kemmerling, and H. Halling, "Comparison of LuYAP, LSO, and BGO as scintillators for high resolution PET detectors," IEEE Trans. Nucl. Sci. **50**, 1370–1372 (2003).